

## Gold mesoflower arrays with sub-10 nm intraparticle gaps for highly sensitive and repeatable surface enhanced Raman spectroscopy

This article has been downloaded from IOPscience. Please scroll down to see the full text article.

2012 Nanotechnology 23 165604

(<http://iopscience.iop.org/0957-4484/23/16/165604>)

View [the table of contents for this issue](#), or go to the [journal homepage](#) for more

Download details:

IP Address: 132.206.27.25

The article was downloaded on 19/08/2012 at 10:56

Please note that [terms and conditions apply](#).

# Gold mesoflower arrays with sub-10 nm intraparticle gaps for highly sensitive and repeatable surface enhanced Raman spectroscopy

Cuifeng Tian<sup>1</sup>, Zhen Liu<sup>1</sup>, Jiehong Jin<sup>2</sup>, Sergei Lebedkin<sup>2</sup>,  
Cheng Huang<sup>2</sup>, Hongjun You<sup>1</sup>, Rui Liu<sup>1</sup>, Liqun Wang<sup>1</sup>, Xiaoping Song<sup>1</sup>,  
Bingjun Ding<sup>1</sup>, Stefan Walheim<sup>2</sup>, Thomas Schimmel<sup>2</sup> and Jixiang Fang<sup>1</sup>

<sup>1</sup> School of Science, MOE Key Laboratory for Nonequilibrium Synthesis and Modulation of Condensed Matter, Xi'an Jiaotong University, Xi'an, People's Republic of China

<sup>2</sup> Karlsruhe Institut für Technologie (KIT), Institut für Nanotechnologie, Karlsruhe, Germany

E-mail: [jxfang@mail.xjtu.edu.cn](mailto:jxfang@mail.xjtu.edu.cn)


Received 15 January 2012, in final form 8 March 2012

Published 2 April 2012

Online at [stacks.iop.org/Nano/23/165604](http://stacks.iop.org/Nano/23/165604)

## Abstract

Self-assembling Au mesoflower arrays are prepared using a polymethylmethacrylate (PMMA) template on an iron substrate via a combined top-down/bottom-up nanofabrication strategy. The PMMA template with the holes around 300–500 nm in diameter is first fabricated by using polymer blend lithography on iron substrates, and the highly homogeneous Au mesoflower arrays with less than 10 nm intraparticle gaps are subsequently obtained by an *in situ* galvanic reaction between HAuCl<sub>4</sub> solution and the iron substrate under optimal stirring of the solution as well as reaction time. Owing to the unique mesostructures and uniformity, Raman measurements show that the gold mesoflower arrays obtained demonstrated a strong and reproducible surface enhanced Raman scattering (SERS) enhancement on the order of  $\sim 10^7$ – $10^8$ . The development of a SERS substrate based on the Au mesoflowers with high spatial density of hot spots, relatively low cost and facial synthesis provides a novel strategy for applications in chemical and biomolecular sensing.

 Online supplementary data available from [stacks.iop.org/Nano/23/165604/mmedia](http://stacks.iop.org/Nano/23/165604/mmedia)

(Some figures may appear in colour only in the online journal)

## 1. Introduction

Surface enhanced Raman scattering (SERS)-based signal detection and molecular identification have been intensively investigated in the past decade [1–3], because of having the highest sensitivity among analytical techniques, potentially leading to single-molecule detection [4, 5]. ‘Hot spots’ (or ‘hot sites’) are the regions where the surface plasmons are highly localized in a small volume of the order of a few nm<sup>3</sup>, giving rise to very large SERS enhancements, up to  $\sim 10^{10}$ – $10^{11}$ . Recent investigations indicate that only a small proportion of colloid aggregates (hot particles) seem to

contribute to the main SERS signals; e.g., in [6], the hottest SERS-active sites accounted for only 63 of the 1000 000 total sites, but contributed 24% of the total SERS intensity. In these respects, SERS reproducibility across a substrate is hardly achieved, because each hot spot is quite small in size and possesses low spatial density around the SERS substrate; thus the probability that target analyte molecules adsorb there is very small. Therefore, it is desirable to exploit ultrasensitive, reproducible, and uniform SERS substrates, where hot spots are ideally distributed and easily found under a routine optical microscope.

In order to improve the reproducibility and reliability for the SERS-based molecule detection, many efforts have recently been made using a variety of patterning techniques, such as electron beam lithography (EBL), optical lithography, and nanoimprint lithography, as well as nanosphere lithography [7, 8]. However, these techniques are associated with limitations regarding throughput, cost, and materials that can be processed. Moreover, it is still difficult to fabricate well-controlled small gaps on the scale of less than  $\sim 10$  nm to create the efficient 'hot spots'; therefore only a moderate SERS enhancement ( $\sim 10^5$ – $10^6$ ) is usually attainable [2, 9]. Importantly, the typical spatial density of the 'hot spots' achieved for lithographically produced substrates is relatively low owing to a relatively low density of lithographed units. Consequently, within the small region of a laser spot, e.g., a few micrometers, there is a low probability of finding target analyte molecules that localize in the vicinity of the 'hot spots', particularly at an ultra-low concentration of target molecules, i.e. single-molecule level. In this regard, central to high SERS performance is the maximization of the spatial density of hot spots.

Large values of SERS enhancement have been achieved for a number of substrates synthesized by means of bottom-up techniques, including nanoshells [10], core-shell nanoparticles [11], 'meatball' particles [12], 'flower-like' nanoparticles [13], and nanolenses [14]. A feature common to these nanostructures is the presence of corrugated or creviced regions and sharp structures. These regions make the major contributions to hot spots and play an important part in extremely sensitive SERS according to recent investigations using the techniques of tip enhanced Raman scattering (TERS) [15] and electron energy-loss spectroscopy (EELS) [16]. However, these bottom-up nanostructures suffer from the obvious shortcoming that it is difficult to assemble them into two-dimensional arrays. Exceptionally, the 'sea urchin'-like Au mesoparticles demonstrate a highly repeatable and reproducible SERS signal for a single particle and are capable of self-assembly into dense and extended two-dimensional arrays on the Si substrates over large areas [17]. However, their weak adhesion onto the Si substrate is another drawback which is common to all of the above nanostructures.

Here, with the aim of creating high spatial density of hot spots, and simultaneously keeping the high reliability and reproducibility, a simple and efficient route combining top-down/bottom-up strategies for the fabrication of SERS-active substrates is proposed. We note that in the previous templated assembly work, such as that on 'aperiodic nanogalaxies' [18], 'nanodimers' [19], and Au nanoparticle arrays [20, 21], a template was always pre-prepared by means of EBL or interference lithography: time-consuming and expensive techniques, particularly limited for scaling up to cm dimensions. In this paper, we report a simple top-down template route, combined with a bottom-up galvanic reaction, for fabricating Au mesoflower arrays which exhibit a stable and reproducible SERS enhancement, making them suitable for highly sensitive SERS substrate use. Unlike the fabrication techniques mentioned above, our method has

unique advantages, such as the following: (A) self-assembled patterning by polymer blend lithography is a very facile and cost-saving process; (B) multiple bright and highly spatially dense hot spots can be created, as attributed to the specific mesostructure; and (C) the stable and reproducible SERS signals can be achieved by the uniform mesoflowers.

## 2. Experimental section

### 2.1. Polymer blend lithography

The PMMA template was generated by polymer blend lithography. First, an original polymer film consisting of PS (polystyrene) 'islands' surrounded by a PMMA (polymethylmethacrylate) 'sea' was spin cast from a PS/PMMA (molecular weight: 36 k/9.6 k) (3/7 by weight) solution with the solvent MEK (methyl ethyl ketone). The polymers were purchased from Polymer Standards Services (Mainz, Germany). The total concentration of the polymers in the solution was  $15 \text{ mg ml}^{-1}$ , the spin speed was about 4500 revolutions per minute (rpm) and the relative humidity was regulated at about 40%. After rinsing with cyclohexane, the PS component was dissolved and removed from the film, so only the PMMA template with holes was left on the substrate.

### 2.2. Fabrication of Au mesoflowers

In this paper, we fabricated Au mesoflowers on PMMA template using a facile galvanic reaction between Fe and  $\text{HAuCl}_4$ . The substrate is immersed into the precursor solution ( $1$ – $10 \text{ mmol l}^{-1}$ )  $\text{HAuCl}_4 \cdot 4\text{H}_2\text{O}$  (Kunming Institute of Precious Metals, China) at a constant speed of  $0.85 \text{ mm s}^{-1}$  by using a dip-coating technique in a layer builder (KSV5000-3). At the same time, the solution was stirred gently using a magnetic stirring bar at  $v = 100 \text{ rpm}$ . Then it was remained inside the solution for 30 s, and then was pulled up. The stirring speed and dwell time determined the uniformity and thickness of the growth. Finally, the substrate was washed with ethanol, acetone and distilled water, and dried in a desiccator.

### 2.3. Sample characterization

X-ray powder diffraction (XRD) analysis was carried out using a Bruker D8 ADVANCE x-ray diffractometer with graphite monochromatized  $\text{Cu K}\alpha$  radiation ( $\lambda = 1.5406 \text{ \AA}$ ). A scan rate of  $0.018^\circ \text{ min}^{-1}$  was used to record the patterns in a  $2\theta$  range of  $20^\circ$ – $90^\circ$ .

The morphology of the Au mesoflower was characterized by scanning electron microscopy (SEM, JSM-7000F) and AFM. AFM images were made in the tapping mode with a cantilever from Mikromasch (type NSC15) using a DI Multimode System with an IIIa controller. All samples were imaged under ambient conditions. Raman measurements were performed in backscattering geometry with a LabRAM HR800 confocal Raman microscope at the excitation wavelength of 633 nm. The laser spot on a sample was  $\sim 0.8 \text{ }\mu\text{m}$ . Raman imaging of 'hot spots' over

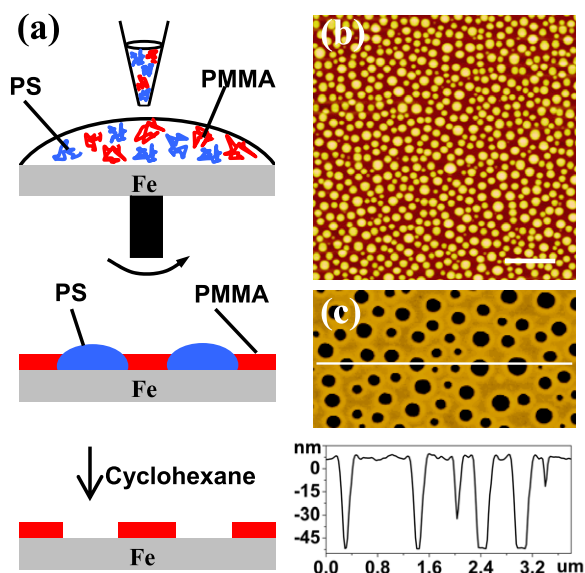


**Figure 1.** (a) Schematic diagrams of the polymer blend lithography used to produce PMMA patterns on Fe substrate. (b) An AFM image shows the resulting pattern of the polymer compound of PS and PMMA. Scale bar: 2  $\mu\text{m}$ . (c) The AFM image of the self-assembled PMMA template after dissolving the PS disks, showing that the thickness of the PMMA template is around 50 nm.

mesoparticle arrays was performed at the same excitation wavelength in backscattering geometry on a WiTec CRM200 confocal Raman microscope employing a piezo-table for sample scanning with a typical X–Y step of 200 nm ( $200 \times 200 \text{ nm}^2$  scanning pixel size), a high-resolution  $100\times$  objective ( $\sim 0.5 \mu\text{m}$  laser spot) and a spectrum acquisition time of 2 s/pixel. The Raman images represent a color-coded area of the characteristic Raman band of CV at  $1172 \text{ cm}^{-1}$  integrated over  $1120\text{--}1250 \text{ cm}^{-1}$  with a subtracted broad background signal.

### 3. Results and discussion

In this study, the PMMA template was fabricated by the polymer blend lithography which had been used in the preparation of the fluoro-decyl-trichlorosilane (FDTs) and amino-silane self-assembled monolayers in our previous work [22]. The process of fabrication of PMMA template is shown in figure 1(a) and described in more detail in supporting information (available at [stacks.iop.org/Nano/23/165604/mmedia](http://stacks.iop.org/Nano/23/165604/mmedia)). Briefly, we chose polystyrene (PS) and PMMA dissolved in methylethyl ketone (MEK) as a polymer blend solution. Firstly, the polymer blend solution was spin cast onto an iron substrate. Secondly, PS disks were selectively dissolved with cyclohexane. In this fashion, an effective PMMA template with a great number of holes surrounded by a PMMA matrix on an Fe substrate was successfully fabricated. An atomic force microscope (AFM) image of the polymer film consisting of PS disks interspersed in the PMMA matrix is illustrated in figure 1(b). The white dots with diameters in the range of  $\sim 500 \text{ nm}$  represent PS disks. The brown region is the PMMA matrix. In figure 1(c),

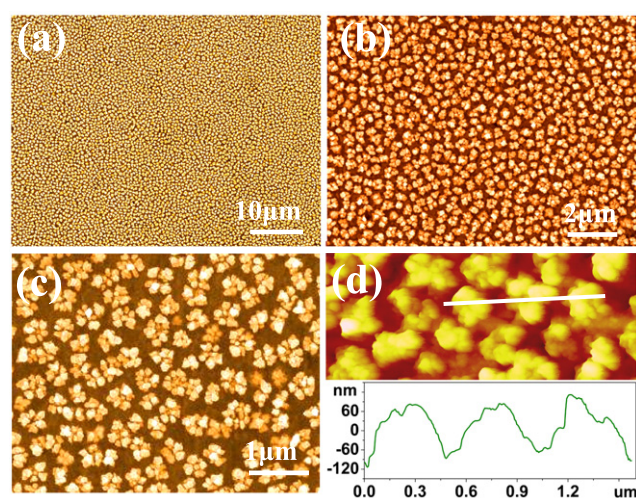


**Figure 2.** Typical SEM images of Au mesoflowers on self-assembled PMMA patterns after the reaction lasted for 30 s at the magnetic stirring speed of 100 rpm. (a) Low magnification image of the specimen 'A'. (b), (c) Magnified SEM images of specimen 'A'. (d) An AFM image and height profile for Au mesoflowers. The position of the line profile is indicated by the white line in the AFM image.

a typical AFM image of PMMA film after the removal of PS is shown. The black dots are the bare iron surface and the yellow region is the PMMA film. The bottom curve of figure 1(c) shows an AFM cross-section profile of the PMMA template along the white line. It is obvious that a 50 nm PMMA thin layer has been obtained. The diameter of the holes is  $\sim 300\text{--}500 \text{ nm}$  with the separation ranging between 400 and 500 nm.

Following the preparation of PMMA template, Au mesoflower arrays were grown *in situ* on Fe substrates using a facile galvanic reaction between Fe and  $\text{HAuCl}_4$ . This simple method has been utilized to prepare highly effective SERS substrates recently [23–25]. This was done by directly dipping the Fe substrate patterned with PMMA film into 10 mM  $\text{HAuCl}_4$  solution by the use of KSV-5000-3 (KSV Instruments, Finland) deposition equipment at a deposition speed of  $0.85 \text{ mm s}^{-1}$ . The substrate was then kept for 30 s in the solution and subsequently pulled out from the solution at the same speed. In the whole process, the solution was stirred by a magnetic stirring bar at the rotating speed of 100 rpm. As a result, Au mesoflower arrays with high uniformity were obtained on the PMMA template (specimen 'A'). The structure and chemical composition of the Au mesoflowers on the PMMA patterned Fe substrate were characterized using x-ray diffraction (XRD) and energy-dispersive x-ray spectroscopy (EDX; figures S1 and S2 in the supporting information available at [stacks.iop.org/Nano/23/165604/mmedia](http://stacks.iop.org/Nano/23/165604/mmedia)). The microstructure of the synthesized Au mesoflowers was investigated by scanning electron microscopy (SEM) and AFM as shown in figure 2. In figure 2(a) and figure S3a (supporting information available at [stacks.iop.org/Nano/23/165604/mmedia](http://stacks.iop.org/Nano/23/165604/mmedia)), the Au mesostructural arrays are quite uniform throughout the whole specimen. From the image of relatively large magnification



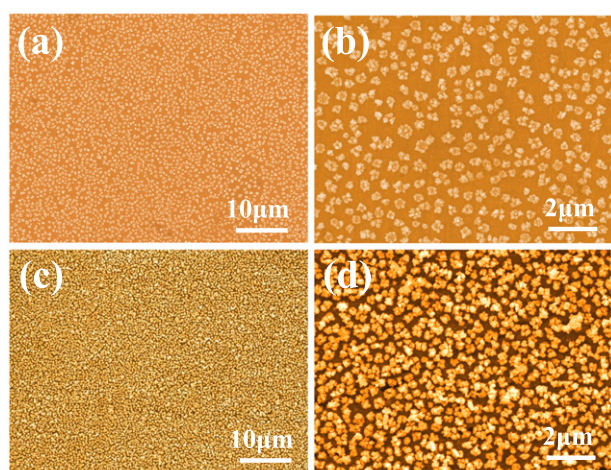


**Figure 3.** (a) Typical SEM images of Au mesoflowers on self-assembled PMMA patterns after the reaction proceeds for 30 s at the magnetic stirring speed of 50 rpm. (b) The magnified image of the specimen 'B' as shown in (a). (c) Typical SEM images of Au mesoflower arrays on self-assembled PMMA patterns after the reaction proceeds for 40 s at the magnetic stirring speed of 100 rpm. (d) The magnified image of the specimen 'C' as shown in (c).

(figure 2(b) and figure S3b available at [stacks.iop.org/Nano/23/165604/mmedia](http://stacks.iop.org/Nano/23/165604/mmedia)), the distance between Au islands is  $\sim 100\text{--}400$  nm and the size of each island is  $\sim 300\text{--}500$  nm. In figure 2(c), it is clear that a gold island is like a mesoflower embedded in each hole of the PMMA template. A magnified image of a single mesoflower is presented in figure 6. In fact, each individual mesoflower consists of many Au nanoparticles with a particle size about 10–40 nm and abundant sub-10 nm nanogaps. A similar highly corrugated and creviced structure has been shown to create very efficient SERS hot spots [15, 16]. The AFM images and height profiles of the Au mesoflowers (shown in figure 2(d)) indicated that the height of the mesoflowers was about 100–150 nm.

It is to be noted that the uniformity of the Au mesoflowers was strongly dependent on the optimal magnetic stirring and reaction time in this work. Without magnetic stirring, even if the concentration of  $\text{HAuCl}_4$  solution and reaction time were the same as for specimen 'A' (figure 2), the substrate obtained still displayed an inhomogeneous pattern of gold mesoflowers, as shown in figure S4 (supporting information available at [stacks.iop.org/Nano/23/165604/mmedia](http://stacks.iop.org/Nano/23/165604/mmedia)). When the stirring speed increased to 50 rpm, the uniformity was improved (specimen 'B'; figure 3(a)). However, the magnified SEM image (figure 3(b) and figure S5 available at [stacks.iop.org/Nano/23/165604/mmedia](http://stacks.iop.org/Nano/23/165604/mmedia)) displays that the distance between Au mesoflowers is larger ( $\sim 1.5$   $\mu\text{m}$ ) than that in specimen 'A'. The schematic diagrams of the solution flow and the concentration field with and without the magnetic stirring are shown in figure 4. In fact, the mass transformation for the current galvanic reaction between the Fe substrate and  $\text{HAuCl}_4$  solution obviously involves a diffusion limited aggregation (DLA) [26]. The existence of a concentration gradient field restricts the supply of the ions to all the nucleation sites; thus an inhomogeneous pattern results (figures 4(a) and (b)). When a magnetic stirring is

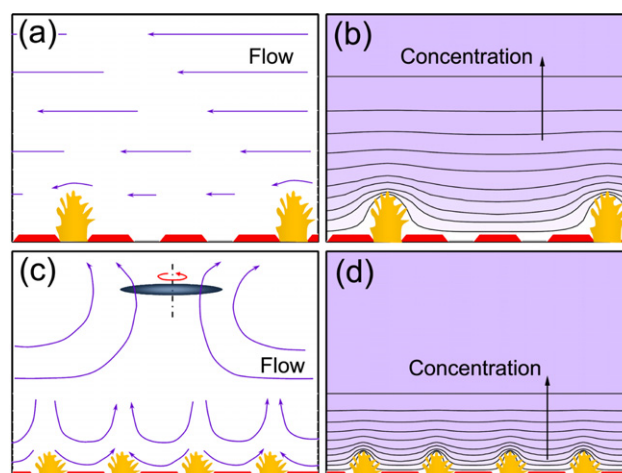


**Figure 4.** The schematic diagram of the solution flow and the concentration field: ((a), (b)) without a magnetic stirring and ((c), (d)) with a magnetic stirring. The arrows represent the flow direction and the length of the arrows represents the flowing speed. The turbulence in (c) was created by the magnetic stirring and thus decreases the diffusion layer thickness of the concentration field.

introduced, the external agitation breaks the distribution of the concentration field or reduces the thickness of the diffusion layer (figures 4(c) and (d)). Therefore, a homogeneous ion supply to all sites of bare Fe contributes to the final uniform Au mesoflower arrays. In this procedure, the reaction time can also be an important factor in the formation of a uniform mesoflower array. When the reaction time reached  $\sim 40$  s, even keeping the same stirring speed, i.e. 100 rpm, as for specimen 'A', the coarsening of the gold mesoflowers can also be observed, as shown in figures 3(c) and (d) (specimen 'C'). Probably the Ostwald ripening or defocusing process can happen during the above coarsening (which is similar to the result of our previous work [27, 28]), forming an inhomogeneous mesoflower pattern.

The SERS sensitivity of these substrates was tested using crystal violet (CV) molecules. The enhancement factors (EFs) of the Au mesoflower arrays were estimated on the basis of [29, 30]

$$\text{EF} = \frac{I_{\text{surface}}/N_{\text{surface}}}{I_{\text{solution}}/N_{\text{solution}}}$$

where  $N_{\text{solution}}$  and  $N_{\text{surface}}$  are the numbers of probed molecules in a reference solution and on the mesoflowers, and  $I_{\text{solution}}$  and  $I_{\text{surface}}$  correspond to the normal and SERS signal intensities, respectively. The measurements of the Raman signal intensities were performed using a LabRAM HR800 Raman spectrometer with a 633 nm laser as the excitation source. The laser beam size focused on the samples was  $\sim 0.8$   $\mu\text{m}$  in diameter under confocal mode. Raman signals were collected through the same objective in the backscattering geometry. An extremely low incident laser power ( $\sim 0.05$  mW) was used in order to minimize heating and photochemical effects during SERS measurements. The acquisition time was 20 s. The curves A, B, C in figure 5 demonstrate the Raman spectra from CV molecules adsorbed on the specimens 'A', 'B' and 'C', respectively. The SERS

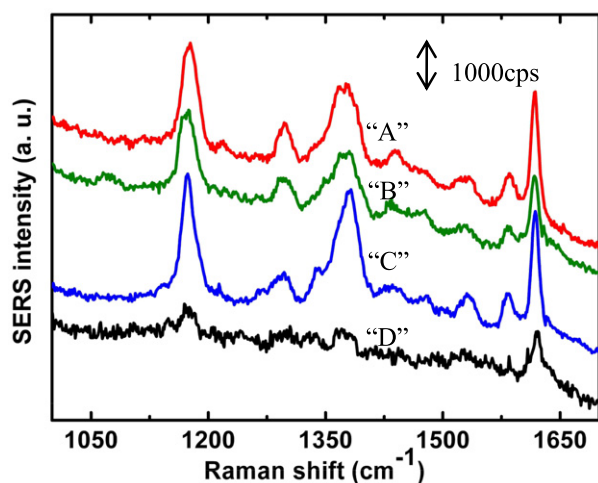


**Figure 5.** SERS spectra of CV on different substrates: specimens 'A', 'B' and 'C'. The spectra were measured at the CV concentration of  $5 \times 10^{-8}$  M and excitation wavelength of 633 nm. The bottom curve 'D' is a Raman spectrum obtained from CV with the concentration of  $10^{-4}$  M deposited on glass.

spectra reveal the main vibrational features of CV molecules: the positions and relative intensities of three peaks at 1172, 1371, and 1619  $\text{cm}^{-1}$ , respectively, and correspond well to the ordinary Raman spectrum of CV (curve 'D' in figure 5). The peak intensities of CV molecules are around  $\sim 1610$ ,  $\sim 1260$  and  $\sim 2030$  counts on the above three SERS substrates at  $\sim 1172$   $\text{cm}^{-1}$ , respectively. The number of probed molecules, one of the crucial parameters for the enhancement factor, was estimated via the geometrical factors of the sample and the quantities of CV molecules within the light spot (see the details in the supporting information available at [stacks.iop.org/Nano/23/165604/mmedia](http://stacks.iop.org/Nano/23/165604/mmedia)). In the calculation of the EF, we supposed about 10% of CV molecules to remain after rinsing the substrate [31], so this may be the source of error. If all the CV molecules remain on the surface, the EF is calculated as  $\sim 10^6$ . In fact, the CV molecules will run out of the surface, largely. If only 1% remain, then the EF is about  $10^8$ . According this, the error range of the EF estimates is about 10%. According to the calculations of EFs described in [17, 29, 30], for the peak at 1172  $\text{cm}^{-1}$  for CV molecules, we estimated EFs of about  $\sim 10^7$ – $10^8$  for specimens, 'A', 'B' and 'C', respectively. It should be noted that the aggregation of mesostructural nanoparticles may strongly influence the microstructures of Au mesoflowers. According to the conclusions for the nanogap effect demonstrated in [32], the SERS enhancement becomes stronger with nanogap size decreasing from 50 to less than 10 nm. So the presence of creviced regions between different nanoparticles, i.e.  $< 10$  nm gaps, or corrugated morphologies on the surface of individual nanoparticles can contribute to the creation of abundant 'hot spots' which mainly determine the sensitivity of the SERS substrate. Figure 6 demonstrates the typical morphology of the synthesized Au mesoflower on an Fe substrate. One can clearly see that an individual mesoflower is composed of some large particles (some tens), 100–200 nm in diameter. Some sub-10 nm gaps are created during the aggregation of

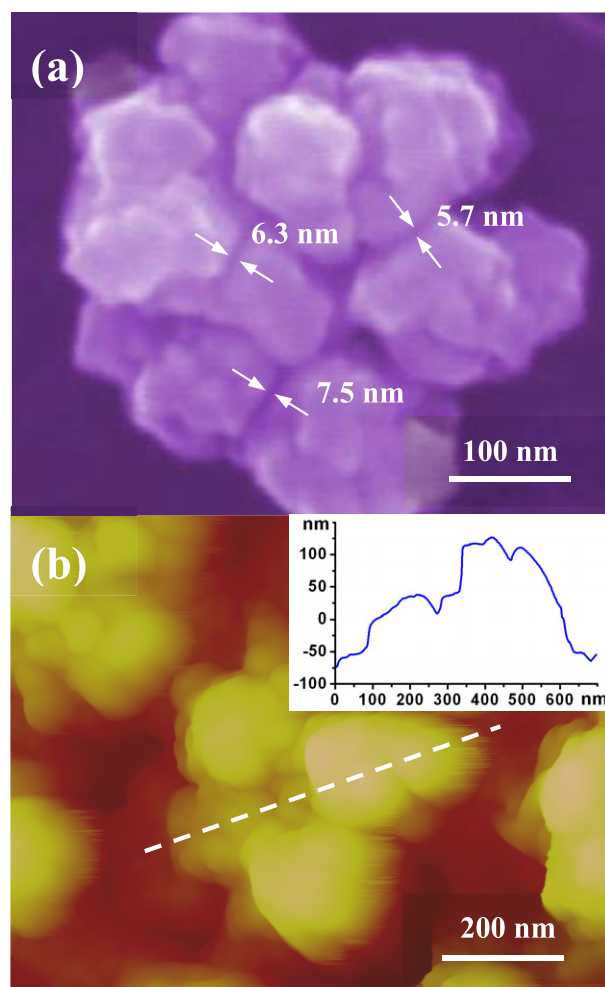


**Figure 6.** (a) A magnified SEM image of the Au mesoflower. (b) An AFM image of Au mesoflowers and the height profile (inset). The position of the line profile is indicated by the white line in the AFM image.

these large particles, as shown in figure 6(a). Furthermore, some corrugated microstructures can also be observed on the surface of individual large particles, which prove that the growth of the Au flower-like nanostructures undergoes a mesoscale aggregation process as reported in our previous experiments [33–36]. In fact, the roughened nature of the Au mesoflowers obtained can also be supported from the AFM image and its cross-section profile as shown in figure 6(b). Thus, these unique microstructures are suggested to strongly influence the sensitivity of the SERS substrate of the Au mesoflower arrays. In this study, on the other hand, the less densely packed morphology of the specimen 'B' (figure S5 available at [stacks.iop.org/Nano/23/165604/mmedia](http://stacks.iop.org/Nano/23/165604/mmedia)) and the coarsening aggregation of the nanoparticles in the specimen 'C' (figures 3(c) and (d)) would be disadvantageous as regards achieving a high sensitivity, which is attributed to the reduction of effective 'hot spots'.

To further evaluate the homogeneity and stability of SERS signals for the above Au mesoflower arrays with various aggregations, we have analyzed them by taking the SERS spectra of CV molecules at different occasional array

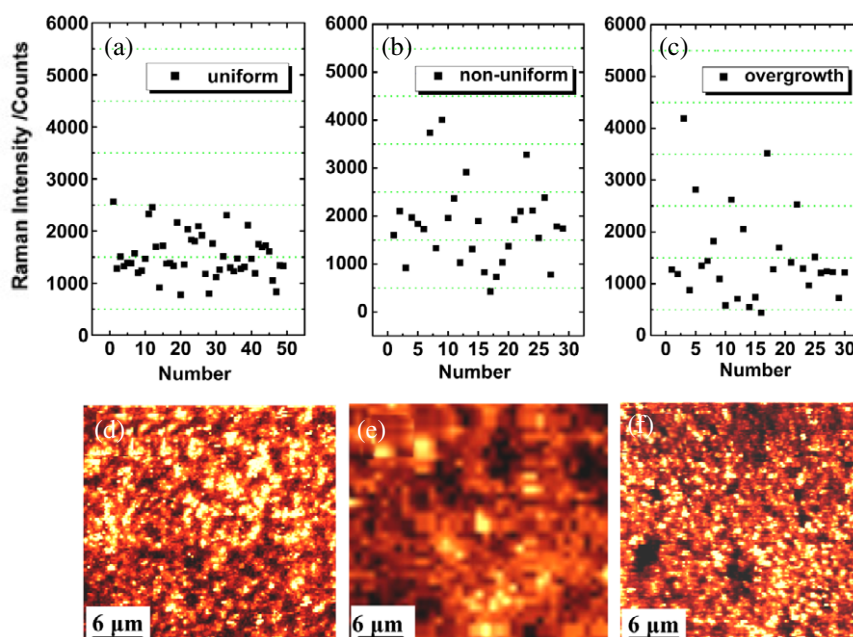


**Figure 7.** (a) Scatter diagrams for the peak height of  $1172\text{ cm}^{-1}$  for the 49 SERS spectra obtained from CV on the specimen 'A', and ((b), (c)) for the 30 SERS spectra obtained from CV on the specimens 'B' and 'C'. ((d)–(f)) Raman images of Au mesoflower arrays for specimens 'A', 'B' and 'C', respectively, displaying a color-coded area obtained by mapping the CV Raman peak at  $\sim 1172\text{ cm}^{-1}$ .

locations as well as the SERS images of 'hot spots' over self-assembled Au mesoflower arrays. Figures 7(a)–(c) are the scatter diagrams of the  $1172\text{ cm}^{-1}$  peak intensity in the SERS spectra for specimens 'A', 'B' and 'C', respectively. One can clearly see that the distribution of the peak intensity is relatively narrow for the specimen 'A' (figure 7(a)). In contrast, the distributions of the peak intensities for specimens 'B' and 'C' are relatively dispersed (figures 7(b) and (c)). In the measurement of Raman signals for the three samples, we choose gold yellow areas on the substrate to measure. However, from another perspective, that of the objective movement distance, samples 'A' and 'C' are different from 'B', for which the distance between Au mesoflowers is larger than that for 'A' and 'C'. From this point, if we measure the intensity of the Raman signal at the same spatial distance, we would see that the averaged intensity for specimen 'A' is larger than that for 'B'. So we think that the uniform specimen is better than the non-uniform specimen. This can be further supported through a statistical analysis of the SERS data. For the above three substrates, the relative standard deviations of the peak intensities in the SERS spectra of CV are 28.1%, 49% and 66.8%, respectively. The superior homogeneity of the uniform Au mesoflower arrays in specimen 'A' is further supported by SERS images of 'hot spots' over self-assembled arrays. Figures 7(d)–(f) show such images for specimens, 'A', 'B' and 'C' acquired with a lateral resolution of  $\sim 0.5\text{ }\mu\text{m}$ . It is clearly seen that the 'hot spots' over the Au mesoflower arrays of specimen 'A' are the most uniform and abundant.

#### 4. Conclusion

In this work, using a combined top-down/bottom-up nanofabrication strategy, we have demonstrated the preparation of

Au mesoflower arrays on PMMA patterned iron substrates. The reliability and reproducibility of the SERS signals were analyzed using CV molecules as probes, via statistical counting of the SERS intensity and the acquisition of SERS images across the substrates. Raman measurements showed that the gold mesoflower arrays obtained, likely due to the unique mesostructures and interparticle effect, demonstrated a strong and highly reproducible SERS enhancement on the order of  $\sim 10^7$ . The current strategy is a very facile and cost-saving route and can be exploited to prepare various nanostructured patterns for different applications.

#### Acknowledgments

J X Fang was supported by the National Natural Science Foundation of China (No. 51171139), Tengfei Talent Project of Xi'an Jiaotong University, the New Century Excellent Talents in University (NCET), the Doctoral Fund for New Teachers (No. 20110201120039) and the Fundamental Research Funds for the Central Universities (No. 08142008).

#### References

- [1] Li J F *et al* 2010 Shell-isolated nanoparticle-enhanced Raman spectroscopy *Nature* **464** 392–5
- [2] Smythe E J, Dickey M D, Bao J M, Whitesides G M and Capasso F 2009 Optical antenna arrays on a fiber facet for *in situ* surface-enhanced Raman scattering detection *Nano Lett.* **9** 1132–8
- [3] Fofang N T, Park T H, Neumann O, Mirin N A, Nordlander P and Halas N J 2008 Plexcitonic nanoparticles: plasmon–exciton coupling in nanoshell—J-aggregate complexes *Nano Lett.* **8** 3481–7
- [4] Kneipp K, Wang Y, Kneipp H, Perelman L T, Itzkan I, Dasari R R and Feld M S 1997 Single molecule detection



- using surface-enhanced Raman scattering (SERS) *Phys. Rev. Lett.* **78** 1667–70
- [5] Nie S and Emory S R 1997 Probing single molecules and single nanoparticles by surface-enhanced Raman scattering *Science* **275** 1102–6
  - [6] Fang Y, Seong N-H and Dlott D D 2008 Measurement of the distribution of site enhancements in surface-enhanced Raman scattering *Science* **321** 388–92
  - [7] Wang H, Levin C S and Halas N J 2005 Nanosphere arrays with controlled sub-10 nm gaps as surface-enhanced Raman spectroscopy substrates *J. Am. Chem. Soc.* **127** 14992–3
  - [8] Lu Y, Liu G L, Kim J, Mejia Y X and Lee L P 2005 Nanophotonic crescent moon structures with sharp edge for ultrasensitive biomolecular detection by local electromagnetic field enhancement effect *Nano Lett.* **5** 119–24
  - [9] Zhang X, Hicks E M, Zhao J, Schatz G C and Van Duyne R P 2005 Electrochemical tuning of silver nanoparticles fabricated by nanosphere lithography *Nano Lett.* **5** 1503–7
  - [10] Oldenburg S J, Jackson J B, Westcott S L and Halas N J 1999 Infrared extinction properties of gold nanoshells *Appl. Phys. Lett.* **75** 2897–9
  - [11] Jackson J B and Halas N J 2004 Surface-enhanced Raman scattering on tunable plasmonic nanoparticle substrates *Proc. Natl Acad. Sci.* **101** 17930–5
  - [12] Wang H and Halas N J 2008 Mesoscopic Au ‘meatball’ particles *Adv. Mater.* **20** 820–5
  - [13] Liang H Y, Li Z P, Wang W Z, Wu Y S and Xu H X 2009 Highly surface-roughened ‘flower-like’ silver nanoparticles for extremely sensitive substrates of surface-enhanced Raman scattering *Adv. Mater.* **21** 4614–8
  - [14] Kneipp J, Li X, Sherwood M, Panne U, Kneipp H, Stockman M I and Kneipp K 2008 Gold nanolenses generated by laser ablation-efficient enhancing structure for surface enhanced Raman scattering analytics and sensing *Anal. Chem.* **80** 4247–51
  - [15] Pettinger B, Ren B, Picardi G, Schuster R and Ertl G 2004 Nanoscale probing of adsorbed species by tip-enhanced Raman spectroscopy *Phys. Rev. Lett.* **92** 096101
  - [16] Nelayah J, Kociak M, Stéphan O, Abajo F J G, Tencé M, Henrard L, Taverna D, Pastoriza-Santos I, Liz-Marzán L M and Colliex C 2007 Mapping surface plasmons on a single metallic nanoparticle *Nature Phys.* **3** 348–53
  - [17] Fang J X, Du S Y, Lebedkin S, Li Z Y, Kruk R, Kappes M and Hahn H 2010 Gold mesostructures with tailored surface topography and their self-assembly arrays for surface-enhanced Raman spectroscopy *Nano Lett.* **10** 5006–13
  - [18] Gopinath A, Boriskina S V, Premasiri W R, Ziegler L, Reinhard B M and Negro L D 2009 Plasmonic nanogalaxies: multiscale aperiodic arrays for surface-enhanced Raman sensing *Nano Lett.* **9** 3922–9
  - [19] Alexander K D, Hampton M J, Zhang S P, Dhawan A, Xu H X and Lopeza R 2009 A high-throughput method for controlled hot-spot fabrication in SERS-active gold nanoparticle dimmer arrays *J. Raman Spectrosc.* **40** 2171–5
  - [20] Liberman V, Yilmaz C, Bloomstein T M, Somu S, Echegoyen Y, Busnaina A, Cann S G, Krohn K E, Marchant M F and Rothschild M 2010 A nanoparticle convective directed assembly process for the fabrication of periodic surface enhanced Raman spectroscopy substrates *Adv. Mater.* **22** 4298–302
  - [21] Yan B, Thubagere A, Premasiri W R, Ziegler L D, Negro L D and Reinhard B M 2009 Engineered SERS substrates with multiscale signal enhancement: nanoparticle cluster arrays *ACS Nano* **3** 1190–202
  - [22] Bauermann L P, Gerstel P, Bill J, Walheim S, Huang C, Pfeifer J and Schimmel T 2010 Templated self-assembly of ZnO films on monolayer patterns with nanoscale resolution *Langmuir* **26** 3774–8
  - [23] Hao J M, Xu Z H, Han M J, Xu S Y and Meng X G 2010 Surface-enhanced Raman scattering analysis of perchlorate using silver nanofilms deposited on copper foils *Colloids Surf. A* **366** 163–9
  - [24] Gutés A, Carraro C and Maboudian R 2010 Silver dendrites from galvanic displacement on commercial aluminum foil as an effective SERS substrate *J. Am. Chem. Soc.* **132** 1476–7
  - [25] Betz J F, Cheng Y and Rubloff G W 2012 Direct SERS detection of contaminants in a complex mixture: rapid, single step screening for melamine in liquid infant formula *Analyst* **137** 826–8
  - [26] Chazalviel J N 1990 Electrochemical aspects of the generation of ramified metallic electrodeposits *Phys. Rev. A* **42** 7355–67
  - [27] Fang J X, You H J, Ding B J and Song X P 2007 Large-area and high-density gold nanoparticle arrays with sub-10 nm gaps *Electrochem. Commun.* **9** 2423–7
  - [28] Fang J X, Ding B J, Song X P and Han Y 2008 How a silver dendritic mesocrystal converts to a single crystal *Appl. Phys. Lett.* **92** 173120
  - [29] Wang Y, Becker M, Wang L, Liu J Q, Scholz R, Peng J, Gösele U, Christensen S H, Kim D H and Steinhart M 2009 Nanostructured gold films for SERS by block copolymer-templated galvanic displacement reactions *Nano Lett.* **9** 2384–7
  - [30] Cai W B, Ren B, Li X Q, She C X, Liu F M, Cai X W and Tian Z Q 1998 Investigation of surface-enhanced Raman scattering from platinum electrodes using a confocal Raman microscope: dependence of surface roughening pretreatment *Surf. Sci.* **406** 9–22
  - [31] Lee T-W and Gray S K 2005 Subwavelength light bending by metal slit structures *Opt. Express* **13** 9652–9
  - [32] Hatab N A, Hsueh C H, Gaddis A L, Retterer S T, Li J H, Eres G, Zhang Z Y and Gu B H 2010 Free-standing optical gold bowtie nanoantenna with variable gap size for enhanced Raman spectroscopy *Nano Lett.* **10** 4952–5
  - [33] Fang J X, Leufke P M, Kruk R, Wang D, Scherer T and Hahn H 2010 External electric field driven 3D ordering architecture of silver (I) oxide meso-superstructures *Nano Today* **5** 175–82
  - [34] Fang J X, Ding B J and Song X P 2007 Self-assembly mechanism of platelike silver mesocrystal *Appl. Phys. Lett.* **91** 083108
  - [35] Fang J X, You H J, Kong P, Yi Y, Song X P and Ding B J 2007 Dendritic silver nanostructure growth and evolution in replacement reaction *Cryst. Growth Des.* **7** 864–7
  - [36] Fang J X, Ding B J and Song X P 2008 Self-assembly ability of building units in mesocrystal, structural, and morphological transitions in Ag nanostructures growth *Cryst. Growth Des.* **8** 3616–22